Multi-objective Stochastic Optimal Configuration for Device Capacities in Carbon Capture and Power to Gas in Offshore-onshore Integrated Energy System

Shunjiang Lin, Xuan Sheng, Yue Pan, Weikun Liang, and Mingbo Liu

Abstract—**The offshore-onshore integrated energy system (OOIES) comprises offshore gas production platforms, wind farms, and onshore gas-fired combined heat and power plants, facilitating the integrated operation of multiple energy sources. To address the challenge of optimally configuring the device capacities in carbon capture and power to gas (CC-P2G) amid stochastic fluctuations in offshore gas and wind power outputs, this study proposes a multi-objective approximate dynamic programming algorithm. This algorithm solves the multi-objective stochastic optimal configuration for the device capacities in CC-P2G in OOIES by simultaneously optimizing investment and operation costs, wind power curtailment, and carbon emissions. By leveraging value function matrices for multiple objectives to solve the extended Bellman equation, the multi-objective multi-period model is decomposed into a series of multi-objective single-period optimization problems, which are solved recursively. Additionally, a weighted Chebyshev function is introduced to obtain the compromise optimal solution for multi-objective optimization model during each period. A case study of an OOIES confirms the effectiveness and efficiency of the proposed algorithm.**

Index Terms—**Capacity configuration, carbon capture, power to gas, multi-objective stochastic optimization, integrated energy system, weighted Chebyshev function, approximate dynamic programming.**

I. INTRODUCTION

In response to carbon emission peak and carbon neutrality goals and mandatory emission reduction policies in China, energy systems are facing increasing pressure to reduce carbon emissions. The rapid expansion of renewable energy sources, particularly wind and solar power, has introduced considerable uncertainty in energy supply, posing challenges to the secure and economic operation of energy systems. Furthermore, achieving a cost-effective balance between investment costs and carbon reduction targets remains a significant economic challenge for industries. To address these issues, the integration of a carbon capture and power to gas (CC-P2G) setup presents a promising solution. The CC-P2G system comprises electrolyzer cells (ECs), hydrogen storage tanks (HSTs), hydrogen fuel cells (HFCs), methanation reactors (MRs), and carbon capture (CC) cells. The ECs electrolyze water to convert electric energy into hydrogen, while the CC cells capture CO_2, which, together with hydrogen, are used in the MRs to synthesize synthetic natural gas (SNG). This process facilitates the conversion of electric power into gaseous fuel (hydrogen and SNG) and captures CO_2, improving the integration of electric power and gas systems, supporting wind power utilization, and reducing CO_2 emissions. Several actual CC-P2G projects in operation or in planning around the world are listed in Table I.

TABLE I
SEVERAL EXISTING OR PLANNED CC-P2G PROJECTS

Project	Location	Capacity of CO_2 (t/year)	Operation year
George olah plant	Grindavík, Iceland	4500	2009
Audi e-gas	Werlte, Germany	2800	2013
Solar methanol	Augusta, Australia	15000	2023
Madoqua synfuels	Pataias, Portugal	500000	2023

In the shift toward low-carbon energy and efficient resource use in onshore-offshore regions [1], the offshore-onshore integrated energy system (OOIES) integrates various offshore and onshore energy resources, which enhances cascade utilization of the energy. In an OOIES, onshore gas-fired combined heat and power plants (GCHPPs), offshore gas production platforms (OGPPs), offshore wind farms (OWFs), electric power loads, heat loads, gas loads and hydrogen loads connect with each other via electric cables and gas/hydrogen/heat pipelines, with CC-P2G systems serving as the central components for energy conversion and multi-

---

Manuscript received: November 25, 2024; revised: March 6, 2025; accepted: May 30, 2025. Date of CrossCheck: May 30, 2025. Date of online publication: June 19, 2025.

This work was supported by Guangdong Basic and Applied Basic Research Foundation (No. 2023A1515240075) and Smart Grid-National Science and Technology Major Project (No. 2024ZD0802200).

S. Lin (corresponding author), X. Sheng, Y. Pan, W. Liang, and M. Liu are with the School of Electric Power Engineering, South China University of Technology, Guangzhou 510640, China, and they are also with the Guangdong Key Laboratory of Clean Energy Technology, South China University of Technology, Guangzhou 511458, China (e-mail: linshj@scut. edu. cn; 601911447@qq. com; 987727619@qq.com; 3012273545@qq.com; epmbliu@scut.edu.cn).

DOI: 10.35833/MPCE.2024.001260

energy collaboration in the OOIES. Flexible conversion is valid among electricity, heat, gas, and hydrogen, which offers better renewable energy utilization, lower carbon emission, and higher economic benefits. Optimal configuration for device capacities (OCDC) in CC-P2G can significantly enhance the low-carbon and cost-effective operation of the OOIES. However, the uncertain energy outputs from OWFs and OGPPs affect the energy supply and the process of the OOIES, which presents challenges in determining the configuration for device capacities in CC-P2G [2].

Current research on the OCDC in integrated energy systems (IESs) is extensive. In [3], a two-stage operation model for power to gas (P2G) devices is proposed, analyzing the effect of carbon trading mechanisms on the optimal capacity configuration in P2G devices of IES. In [4], the OCDC for energy storage systems in IES is addressed using the cat swarm optimization algorithm. However, [3] and [4] focus on a single optimization objective, neglecting the need for multiple optimization objectives that balance the economy and low carbon emissions. In [5], a multi-objective optimization model is introduced to optimize gas turbine capacity in energy hubs. Similarly, a multi-objective OCDC of IES model is developed in [6], which employs the heat-determined electricity principle and applies a non-dominated sorting genetic algorithm to obtain the Pareto optimal solution (POS). In [7], a novel multi-objective optimization framework is proposed for uncertain IES planning with demand response, using a coevolutionary algorithm for efficient problem-solving. Additionally, [8] employs a preference selection mechanism to improve the solution for large-scale, discrete, multi-objective bi-layer OCDC. Despite these advancements, no studies have specifically addressed the OCDC in CC-P2G, which is crucial in linking onshore and offshore subsystems in an OOIES. The OCDC in CC-P2G of OOIES must account for multiple conflicting objectives, such as investment costs, carbon emissions, and renewable energy integration. Furthermore, due to the uncertain energy outputs from OGPPs and OWFs, the OCDC in CC-P2G of OOIES should be treated as a multi-objective stochastic optimization (MOSO) problem, which presents significant challenges in finding an efficient solution.

Current solution methods for MOSO problems have been extensively researched, encompassing both MOSO algorithms [9]-[12] and multi-objective robust optimization (MORO) algorithms [13]-[15]. For MOSO algorithms, [9] introduces an unscented transformation-based mean-standard model to account for uncertainties in wind and solar power in IES using multiple scenarios. In [10], an MOSO model for microgrids is developed based on the chance-constrained programming method, using a membership function to determine the optimal weights for the multi-objective problem. In [11], multi-objective interval variables are used, and a group search optimization method is introduced to finalize unit sizing. In [12], dynamic Bayesian networks are used to model gas price fluctuations, and the epsilon constraint method is applied to solve the MOSO problem of IES. However, MOSO algorithms are computationally demanding and time-intensive. In contrast, MORO algorithms, such as the multi-objective bi-level robust optimization model based on the confidence gap decision theory [13], efficiently address renewable energy uncertainties. Another study proposes OCDC combining fuzzy decision-making with two-stage adaptive robust optimization to convert the multi-objective problem into a single-objective one [14]. In [15], economic cost, carbon emissions, and energy supply reliability are considered, leading to the development of an MORO model for the OCDC in IES. However, MORO, much like robust optimization, emphasizes the extreme case of uncertainty, frequently leading to cautious decision-making. Additionally, the existing MOSO algorithms require solving numerous discrete POSs to determine the compromise optimal solution (COS), which lowers computational efficiency and produces an incomplete Pareto frontier, thus reducing the quality of the COS. Thus, further research is needed to address the limitations of MOSO and MORO and develop more reliable and efficient methods for obtaining a high-quality multi-objective COS.

The OCDC in CC-P2G of OOIES is a multi-objective multi-period optimization problem involving stochastic variables. Based on the Bellman's principle of optimality [16], approximate dynamic programming (ADP) enables the decomposition of a multi-period decision problem into sequential single-period subproblems [17], which can then be solved recursively. This method mitigates the inefficiency typically caused by large-scale decision spaces in multi-objective multi-period optimization problems [18]. By accounting for the transition probabilities of stochastic variables between periods, the precision of decision-making can be improved. While ADP has been increasingly applied to stochastic optimization problems in IES [19]-[21], there has been no research exploring the use of the multi-objective ADP (MOADP) algorithm for solving the multi-objective stochastic OCDC (MOSOCDC) problem in CC-P2G.

To efficiently solve the MOSOCDC problem, this study proposes an MOADP algorithm based on a weighted Chebyshev function. The key contributions are as follows.

1) An MOSOCDC model in CC-P2G of OOIES is developed, accounting for the stochastic fluctuations in OWF power and associated gas (AG) outputs. The model optimizes investment and operation costs, wind power curtailment, and carbon emissions simultaneously.

2) An MOADP algorithm is introduced to solve the MOSOCDC model. Using the matrix form of the Bellman equation, the multi-objective multi-period optimization problem is decoupled into single-period problems and solved recursively with the approximate value function (AVF) matrix. The algorithm leverages the weighted Chebyshev function to quickly solve multi-objective single-period optimization problems. The solution with the smallest Chebyshev distance to the utopia point is identified from the feasible domain as the COS.

The remainder of this paper is arranged as follows. Section II presents the MOSOCDC model in CC-P2G of OOIES. Section III introduces the MOADP algorithm for solving the COS of the MOSOCDC model. Section IV offers a case study on an OOIES. Section V outlines the findings of this study.

II. MOSOCDC MODEL IN CC-P2G OF OOIES

The components and energy flows of an OOIES are illustrated in Fig. 1. The OOIES consists of OGPPs, OWFs, and GCHPPs, each performing specific functions.

1) OGPP is equipped with diesel generators and extracts AG, some of which are stored in the associated gas storage (AGS) while the rest are processed into gas. The gas is supplied to gas-fired generators, gas boilers, and gas loads.

2) OWF is installed with an electric hydrogen production unit (EHPU), where FCs supply power to the OGPP. Hydrogen produced by ECs is sent to heat storage (HS), hydrogen loads, and MR in the GCHPP via pipelines.

3) GCHPP contains gas-fired generators converting gas into electricity, with waste heat and gas boilers providing heat to the heat loads. In addition, CO_2 emissions from the gas-fired generators are absorbed by CC, which reacts with H_2 in the MR to produce SNG, completing the utilization process of CC-P2G energy.

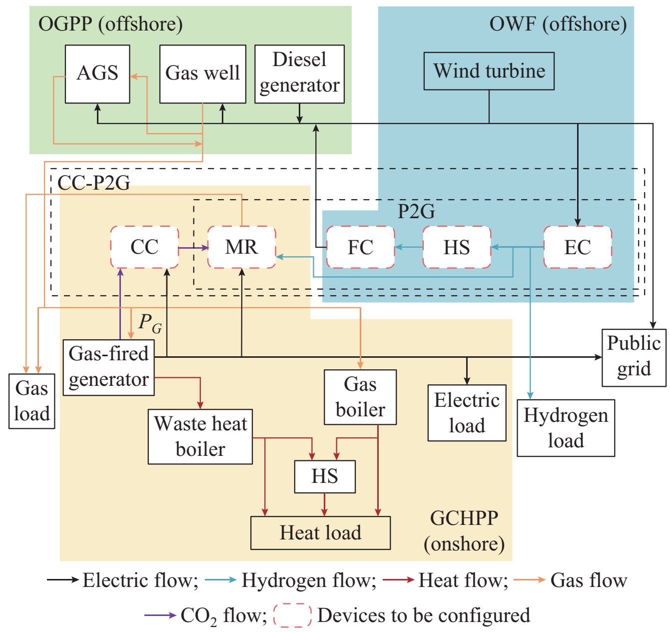

Fig. 1. Components and energy flows of an OOIES.

In an OOIES, the CC-P2G, comprising the EHPU, MR, and CC, serves as the key link for energy conversion and carbon emission reduction. Therefore, the OCDC in CC-P2G is fundamental to the coordinated dispatch of multiple energy sources. To achieve this, the OCDC problem must address the stochastic fluctuations in offshore energy production.

A. Objective Functions

The decision variables for the MOSOCDC model in CC-P2G of OOIES comprise device capacities: the maximum input power of EC P_{EC}, the highest storage energy of HS E_{HS}, the maximum power output of FC P_{FC}, as well as the maximum input power for both the MR P_{MR} and CC device P_{CC}, as shown in (1). To account for the economic and environmental benefits of the system, three optimization objectives are defined: minimizing daily equivalent investment and operation costs, reducing carbon emissions, and minimizing wind power curtailment. The first objective f_1 focuses on economic efficiency, comprising the daily equivalent investment cost of devices C_{inv}, daily maintenance costs of devices C_{m}, and daily energy sale profit C_{s}. C_{inv} is dependent on device capacities, discount rate r, and service life L_{u}. For the HS system, the operating power of device z $P_{z,t}=\varphi_{\mathrm{hyi},t}+\varphi_{\mathrm{hyo},t}$, where $\varphi_{\mathrm{hyi},t}$ and $\varphi_{\mathrm{hyo},t}$ are the input and output flow rates of HSTs, respectively. Considering the higher load levels and stochastic fluctuations in summer, the load and energy production curves of a typical day in summer are used to estimate C_{m} and C_{s}.

$$\boldsymbol{E}_{\Omega}=[P_{\mathrm{EC}},E_{\mathrm{HS}},P_{\mathrm{FC}},P_{\mathrm{MR}},P_{\mathrm{CC}}] \tag{1}$$

$$\begin{cases} \min f_1=C_{\mathrm{inv}}+\sum\limits_{t=1}^{T}C_{\mathrm{m},t}\Delta t-\sum\limits_{t=1}^{T}C_{\mathrm{s},t}\Delta t \\ C_{\mathrm{inv}}=\sum\limits_{z\in\Omega}\left[k_{\mathrm{inv},z}E_z\dfrac{r(1+r)^{L_{\mathrm{u}}}}{(1+r)^{L_{\mathrm{u}}}-1}\right]\Big/M_{\mathrm{s}} \\ C_{\mathrm{m},t}=\sum\limits_{z\in\Omega}k_{\mathrm{m},z}P_{z,t} \\ C_{\mathrm{s},t}=c_{\mathrm{ele}}P_{\mathrm{ele},t}+c_{\mathrm{g}}f_{\mathrm{L},t}+c_{\mathrm{H}}f_{\mathrm{hl},t} \end{cases} \tag{2}$$

where t and T are the index and number of time periods, respectively; Ω is the set of devices to be configured; c_{ele} is the electricity price per unit of electric energy; c_{g} is the gas price; $k_{\mathrm{inv},z}$ and $k_{\mathrm{m},z}$ are the unit investment and maintenance costs of device z in CC-P2G, respectively; Δt is the time period, i.e., 1 hour; M_{s} is the number of days per year, i.e., 365 days; E_z is the configured capacity of device z; $P_{\mathrm{ele},t}$ is the active power output to the public grid; $f_{\mathrm{L},t}$ is the gas load demand; c_{H} is the hydrogen price; and $f_{\mathrm{hl},t}$ is the hydrogen load demand.

The second objective f_2 is to minimize carbon emissions from diesel generators, gas boilers, and gas-fired generators that are not captured by the CC.

$$\min f_2=\sum_{t=1}^{T}[d_{\mathrm{GB}}f_{\mathrm{GB},t}+d_{\mathrm{DG}}P_{\mathrm{DG},t}+(1-\eta_t)\mu_{\mathrm{G}}P_{\mathrm{G},t}]\Delta t \tag{3}$$

where $P_{\mathrm{G},t}$ is the active power output of gas-fired generators; $P_{\mathrm{DG},t}$ is the active power output of diesel generator; d_{GB} and d_{DG} are the carbon emission factors of gas boilers and diesel generators, respectively; μ_{G} is the carbon emission intensity of gas-fired generators; and $f_{\mathrm{GB},t}$ is the input gas flow rate of the gas boiler.

The third objective f_3 is to minimize the total wind power curtailment in OOIES.

$$\min f_3=\sum_{t=1}^{T}\sum_{i\in\Omega_{\mathrm{w}}}(P_{\mathrm{wp}i,t}-P_{\mathrm{w}i,t})\Delta t \tag{4}$$

where i is the index of buses; Ω_{w} is the set of OWF buses; and $P_{\mathrm{wp}i,t}$ and $P_{\mathrm{w}i,t}$ are the maximum available and actual active power outputs of the OWF, respectively.

B. Operation Constraints of Energy Source Output

1) Uncertain Gas Source and OWF Output

The forecasting errors of the extraction mass flow rate of AG from OGPP gas wells $\Delta f_{\mathrm{ag},t}$ and the OWF power output $\Delta P_{\mathrm{wp},t}$ are influenced by small and random factors such as measurement inaccuracies and short-term fluctuations, which are often assumed to obey a Gaussian distribution [22]. Thus, the mass flow rate of AG $f_{\mathrm{ag},t}$ and $P_{\mathrm{wp},t}$ are described as stochastic variables, as modeled in (5) and (6).

$$f_{\mathrm{ag},t}=f_{\mathrm{ag0},t}+\Delta f_{\mathrm{ag},t}\quad \Delta f_{\mathrm{ag},t}\sim Norm(\mu_{\mathrm{f},t},\sigma_{\mathrm{f},t}^2) \tag{5}$$

$$P_{\mathrm{wp},t}=P_{\mathrm{wp0},t}+\Delta P_{\mathrm{wp},t}\quad \Delta P_{\mathrm{wp},t}\sim Norm(\mu_{\mathrm{p},t},\sigma_{\mathrm{p},t}^2) \tag{6}$$

where the subscript 0 indiacates the forecasted value; $\mu_{\mathrm{f},t}$ and $\sigma_{\mathrm{f},t}$ are the mean and standard deviations of the forecasting error of extracted mass flow rate of AG, respectively; $Norm(\cdot)$ denotes the norm distribution; and $\mu_{\mathrm{p},t}$ and $\sigma_{\mathrm{p},t}$ are the mean value and standard deviations of the forecasting errors of the maximum available active power output of OWFs, respectively.

2) GCHPP Output

The energy generation devices in the GCHPP consist of gas-fired generators, waste heat boilers, and gas boilers [23]. The operation constraints for gas-fired generators are outlined in (7). The waste heat from these generators is captured to meet heat loads, with the waste heat boiler output $\varphi_{\mathrm{h},t}$ calculated using (8). The gas boiler generates heat power using gas, with its heat output $\varphi_{\mathrm{GB},t}$ computed in (9).

$$\begin{cases} -R_{\mathrm{dG}}\Delta t \le P_{\mathrm{G},t}-P_{\mathrm{G},t-1}\le R_{\mathrm{uG}}\Delta t \\ \eta_{\mathrm{G},t}=c_{\mathrm{a}}+c_{\mathrm{b}}P_{\mathrm{G},t}^{*}+c_{\mathrm{c}}(P_{\mathrm{G},t}^{*})^2+c_{\mathrm{d}}(P_{\mathrm{G},t}^{*})^3 \\ f_{\mathrm{f},t}=\dfrac{P_{\mathrm{G},t}\rho_{\mathrm{gas}}}{\eta_{\mathrm{G},t}q_{\mathrm{gas}}} \end{cases} \tag{7}$$

where c_{a}, c_{b}, c_{c}, and c_{d} are the efficiency factors of gas-fired generators; R_{uG} and R_{dG} are the maximum ramping up and down rates of gas-fired generators, respectively; $f_{\mathrm{f},t}$ and $\eta_{\mathrm{G},t}$ are the input gas flow rate and efficiency of gas-fired generator, respectively; ρ_{gas} is the gas density; and q_{gas} is the hydrogen calorific value.

$$\varphi_{\mathrm{h},t}=\eta_{\mathrm{WB}}\alpha_{\mathrm{w}}\left(\frac{P_{\mathrm{G},t}}{\eta_{\mathrm{G},t}}-P_{\mathrm{G},t}\right) \tag{8}$$

where α_{w} and η_{WB} are the waste heat ratio and operation efficiency of waste heat boilers, respectively.

$$\varphi_{\mathrm{GB},t}=\eta_{\mathrm{GB}}f_{\mathrm{GB},t}\frac{q_{\mathrm{gas}}}{\rho_{\mathrm{gas}}\Delta t} \tag{9}$$

where η_{GB} is the efficiency of gas boiler.

3) Diesel Generators

To ensure the safe operation of the OGPP, diesel generators provide power for AG extraction. Operation constraints for these generators are detailed in [24].

C. Operation Constraints of CC-P2G Devices

The operation of the CC-P2G system, as shown in Fig. 2, involves an EHPU, which includes the EC, HS, and FC. The EC converts electric power into hydrogen by electrolyzing water. Hydrogen is then partially stored in the HS for future use and partially directed to the FC for power generation, with the remainder of hydrogen sent to the MR for gas synthesis. The CC cell manages post-combustion CO_2: flue gas from gas-fired generators is routed into an absorption tower where it mixes with an amine solution. CO_2 is then separated and transferred to the MR for gas production [25]. The model in [26] focuses on the energy conversion relationship of CC-P2G, which is applied in the proposed MOSOCDC model.

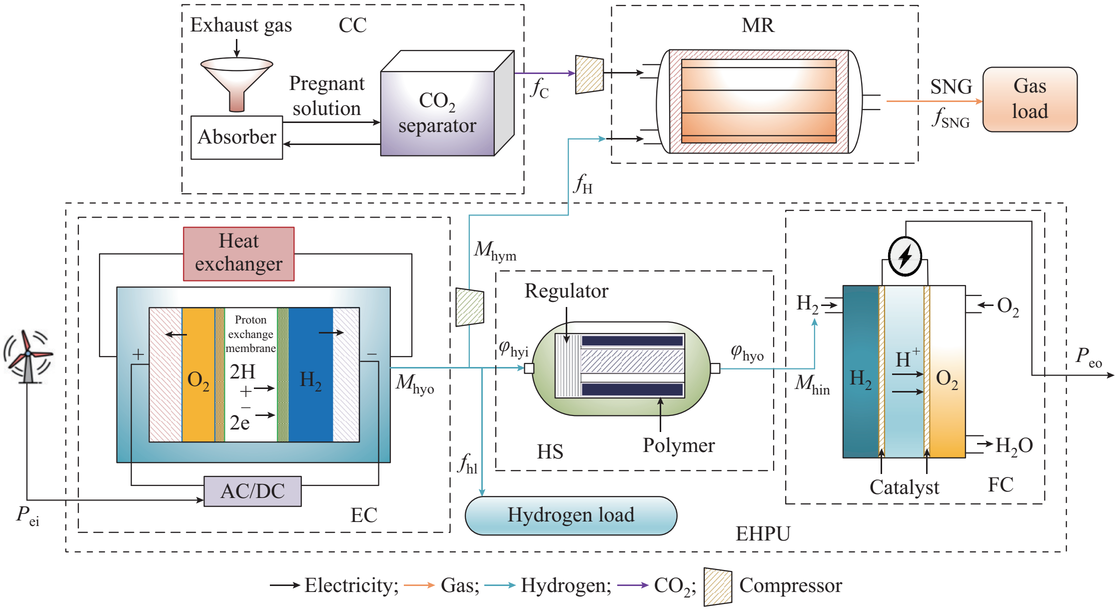

Fig. 2. Schematic of CC-P2G system.

Equation (10) details the constraints for energy conversion of ECs and FCs [23]. The MR produces SNG through the chemical reaction of CO_2 and hydrogen. The operation constraints include both flow rate limitations of SNG derived from chemical equations and power consumption restriction (12) [23], where 4/11 and 11/2 are the constants obtained from the mass conservation in the chemical equation of synthesizing SNG.

$$\begin{cases} M_{\mathrm{hyo},t}=\eta_{\mathrm{el}}P_{\mathrm{ei},t} \\ P_{\mathrm{eo},t}=\eta_{\mathrm{fc}}M_{\mathrm{hyi},t} \end{cases} \tag{10}$$

where $M_{\mathrm{hyo},t}$ and $P_{\mathrm{ei},t}$ are the hydrogen mass flow rate and electric power input of electrolyzers, respectively; $M_{\mathrm{hyi},t}$ and $P_{\mathrm{eo},t}$ are the hydrogen mass flow rate and electric power output of FC, respectively; and η_{el} and η_{fc} are the electro-hydrogen conversion factors of electrolyzers and FCs, respectively.

$$\begin{cases} E_{\mathrm{hy},t+1}=E_{\mathrm{hy},t}(1-\eta_{\mathrm{hy}})+\varphi_{\mathrm{hyi},t}\eta_{\mathrm{hyi}}\Delta t-\dfrac{\varphi_{\mathrm{hyo},t}\Delta t}{\eta_{\mathrm{hyo}}} \\ E_{\mathrm{hy}0}=E_{\mathrm{hy}T} \\ E_{\mathrm{hy,min}}\le E_{\mathrm{hy},t}\le E_{\mathrm{HS}} \\ M_{\mathrm{hin},t}=\eta_{\mathrm{tr2}}\varphi_{\mathrm{hyo},t} \\ \varphi_{\mathrm{hyi,min}}\le\varphi_{\mathrm{hyi},t}\le\varphi_{\mathrm{hyi,max}} \\ \varphi_{\mathrm{hyo,min}}\le\varphi_{\mathrm{hyo},t}\le\varphi_{\mathrm{hyo,max}} \\ \varphi_{\mathrm{hyi},t}=\eta_{\mathrm{tr1}}\left(M_{\mathrm{hyo},t}-M_{\mathrm{hym},t}-\dfrac{f_{\mathrm{hl}}q_{\mathrm{h}}}{\rho_{\mathrm{h}}\Delta t}\right) \end{cases} \tag{11}$$

where η_{hyi} and η_{hyo} are the input and output hydrogen efficiencies of HSTs, respectively; $\varphi_{\mathrm{hyi},t}$ and $\varphi_{\mathrm{hyo},t}$ are the input power and output power of hydrogen storage, respectively; η_{tr1} and η_{tr2} are the efficiencies of hydrogen transfer between electrolyzer to HSTs and HSTs to FC, respectively; η_{hy} is the hydrogen storage loss rate; $M_{\mathrm{hym},t}$ is the input hydrogen power of MR; ρ_{h} is the hydrogen density; q_{h} is hydrogen calorific value; and $E_{\mathrm{hy},t}$ is the remaining hydrogen in HSTs. The parameters with subscripts max and min indicate the upper and lower bounds of the variable.

$$\begin{cases} f_{\mathrm{SNG},t}=\dfrac{4}{11}f_{\mathrm{C},t}\eta_{\mathrm{SNG}} \\ f_{\mathrm{C},t}=\dfrac{11}{2}f_{\mathrm{H},t} \\ P_{\mathrm{mr},t}=f_{\mathrm{SNG},t}\mu_{\mathrm{mr}} \end{cases} \tag{12}$$

where μ_{mr} is the electric power consumption factor of MR; η_{SNG} is the operation efficiency of MR; $f_{\mathrm{C},t}$ is the CO_2 flow rate captured by CC; $f_{\mathrm{H},t}$ is the input hydrogen flow rate of MR; and $f_{\mathrm{SNG},t}$ is the output gas flow rate of MR.

Hydrogen energy is expressed in MWh to align with electric power units. The energy conversion rule is that 1 m^3 of hydrogen at 0 °C and one standard atmospheric pressure have an approximate energy equivalent of 2.95 kWh.

The configuration for CC devices in the GCHPP is essential for reducing carbon emissions from gas-fired generators. The power consumed by CC devices $P_{\mathrm{cc},t}$ includes the electricity used for CO_2 capture and the constant intrinsic power requirements of the device. $f_{\mathrm{C},t}$ and CO_2 released into the atmosphere $f_{\mathrm{em},t}$ are calculated using (13) [23].

$$\begin{cases} P_{\mathrm{cc},t}=p_{\mathrm{Ce}}f_{\mathrm{C},t}+P_{\mathrm{Cb}} \\ f_{\mathrm{C},t}=\eta_{\mathrm{C}}\mu_{\mathrm{G}}P_{\mathrm{G},t} \\ f_{\mathrm{em},t}=\mu_{\mathrm{G}}P_{\mathrm{G},t}-f_{\mathrm{C},t} \end{cases} \tag{13}$$

where p_{Ce} is the electric power consumption factor of CO_2 capture; P_{Cb} is the constant term of electric power consumption of CC system; and η_{C} is the CO_2 capture ratio of CC system.

The allowable maximum and minimum configured device capacity limits for the CC-P2G of OOIES are given in (14). The elements of vector $\boldsymbol{E}_{\Omega}$ are shown in (1).

$$\boldsymbol{E}_{\Omega,\mathrm{min}}\le\boldsymbol{E}_{\Omega}\le\boldsymbol{E}_{\Omega,\mathrm{max}} \tag{14}$$

D. Operation Constraints of Energy Storage Devices and Energy Supply Networks

1) AGS

AGS, constructed from decommissioned gas wells, provides AG to meet load demands when the gas supply exceeds the demand. Maintaining AGS operation requires electric power, as shown in (15) and (16).

$$\begin{cases} E_{\mathrm{ag},t+1}=E_{\mathrm{ag},t}+\eta_{\mathrm{agi}}f_{\mathrm{agi},t}\Delta t-\dfrac{f_{\mathrm{ago},t}\Delta t}{\eta_{\mathrm{ago}}} \\ E_{\mathrm{ag}0}=E_{\mathrm{ag}T} \\ E_{\mathrm{ag,min}}\le E_{\mathrm{ag},t}\le E_{\mathrm{ag,max}} \\ f_{\mathrm{agi,min}}\le f_{\mathrm{agi},t}\le f_{\mathrm{agi,max}} \\ f_{\mathrm{ago,min}}\le f_{\mathrm{ago},t}\le f_{\mathrm{ago,max}} \end{cases} \tag{15}$$

$$P_{\mathrm{ag},t}=k_{\mathrm{ag}}(f_{\mathrm{agi},t}+f_{\mathrm{ago},t}) \tag{16}$$

where $E_{\mathrm{ag},t}$ is the remaining gas in AGS; $f_{\mathrm{agi},t}$ and $f_{\mathrm{ago},t}$ are the input and output mass flow rates of AG, respectively; η_{agi} and η_{ago} are the input and output gas efficiencies of AGSs, respectively; and k_{ag} is the electric power consumption factor of AGS.

2) HSTs

HSTs are used to manage discrepancies between heat production and demand. The operation constraints are similar to the 1st, 2nd, and 4th line formulae in (11), with the subscript modified from "hyi/hyo/hy" to "hi/ho/h". Note that the power network [27] and gas network [28] are described in Supplementary Material A.

3) Heat Network

The operation constraints for the heat network include models for nodal thermal power, pipeline temperature, fluid mixing at nodes with multiple branches, and electric power consumed by circulating pumps [28].

4) Upper and Lower Operation Bound Constraints

During the OOIES operation, all device outputs are constrained to operate within their capacity bounds. These boundary conditions are specified by:

$$\begin{cases} \boldsymbol{y}_{\mathrm{min}}\le\boldsymbol{y}_t\le\boldsymbol{y}_{\mathrm{max}} \\ \boldsymbol{y}_t=[P_{\mathrm{ele},t}, Q_{\mathrm{ele},t}, P_{\mathrm{w},t}, f_{\mathrm{GB},t}, p_{\mathrm{h},t}, P_{\mathrm{G},t}, \eta_t, V_{j,t}, \theta_{j,t}, T_{\mathrm{wk},t}, \\ \qquad T_{\mathrm{rk},t}, P_{\mathrm{ei},t}, P_{\mathrm{eo},t}, P_{\mathrm{mr},t}, P_{\mathrm{cc},t}] \end{cases} \tag{17}$$

where $Q_{\mathrm{ele},t}$ is the reactive power output to the public grid; and $T_{\mathrm{wk},t}$ and $T_{\mathrm{rk},t}$ are the supply and return water temperatures of node k, respectively. For the variables $P_{\mathrm{ei},t}$, $P_{\mathrm{eo},t}$, $P_{\mathrm{mr},t}$, and $P_{\mathrm{cc},t}$, the corresponding upper limits in $\boldsymbol{y}_{\mathrm{max}}$ are P_{EC}, P_{FC}, P_{MR}, and P_{CC}, respectively, while their lower limits in $\boldsymbol{y}_{\mathrm{min}}$ are all 0.

Equations (2)-(17) and Supplementary Material A (A1)-(A5) define an MOSOCDC model in CC-P2G of OOIES. Due to the stochastic variations in $P_{\mathrm{wp},t}$ and $f_{\mathrm{ag},t}$, this model is a complex multi-objective mixed-integer non-linear programming challenge with stochastic variables. An MOADP algorithm is presented in this study, which simplifies the original multi-objective multi-period model by decomposing it into multiple single-period subproblems that can be solved recursively. Additionally, a method based on the weighted Chebyshev function is proposed to obtain the COS of each multi-objective single-period optimization problem.

For this three-objective optimization problem, it is crucial to acknowledge the conflicts between the objectives. Reducing wind power curtailment often requires investing in additional CC-P2G devices, which can increase economic costs. Similarly, minimizing carbon emissions typically necessitates more CC-P2G devices, further raising costs. Conversely, minimizing economic costs might involve fewer CC-P2G devices and greater reliance on fossil fuels, which contradicts the objectives of reducing wind power curtailment and carbon emissions. Therefore, it is essential to optimize the three objectives by using a coordinated method. POSs can effectively represent this coordinated optimization across multiple objectives.

III. SOLUTION METHODOLOGY

A. Solution of COS Based on Weighted Chebyshev Function

In multi-objective optimization, many POSs are typically computed first, from which the COS is selected. This process can be time-consuming due to the need to solve these POSs. The challenge lies in efficiently obtaining the COS across multiple objectives. A common method is the reference point method, which involves finding a vector that minimizes the distance to a predefined reference point. By minimizing the weighted Chebyshev function $\psi(\cdot)$, as shown in (18), the COS with a high degree of overall optimization can be achieved by:

$$\psi(\boldsymbol{V},\boldsymbol{r},\boldsymbol{\beta})=\max_{q}\left(\beta_q\left|\boldsymbol{r}-\boldsymbol{V}_q\right|\right) \tag{18}$$

where $\boldsymbol{V}$ is the value function (VF) vector; $\boldsymbol{r}$ is the reference point vector, typically set as the utopia point; $\boldsymbol{\beta}$ is the positive weight vector; β_q is the weight of the q^{th} objective function; and $\left|\boldsymbol{r}-\boldsymbol{V}_q\right|$ is the Euclidean distance between the two vectors.

The structure of the ω-objective optimization model is defined in (19). Initially, ω single-objective optimization (SOO) solutions are solved individually. Let $\boldsymbol{V}_p^*$ represent the optimal objective function values for the p^{th} SOO solution and V_p^{q*} signify its value for the q^{th} objective function. The $\omega\times\omega$ dimension payment matrix is constructed as shown in (20). $\boldsymbol{r}$ is defined as $\boldsymbol{r}=[V_1^*,V_2^*,\dots,V_\omega^*]$, $\boldsymbol{V}_q$ is defined as $\boldsymbol{V}_q=[V_1^{q*},V_2^{q*},\dots,V_p^{q*},\dots,V_\omega^{q*}]$, and the nadir point $\boldsymbol{a}$ is a vector defined as $\boldsymbol{a}=(\max(V_p^{1*}),\max(V_p^{2*}),\dots,\max(V_p^{\omega*}))$.

$$\min\left\{f_1(y),f_2(y),\dots,f_\omega(y)\right\} \tag{19}$$

$$\begin{bmatrix} f_1(y^{1*}) & f_2(y^{1*}) & \cdots & f_\omega(y^{1*}) \\ f_1(y^{2*}) & f_2(y^{2*}) & \cdots & f_\omega(y^{2*}) \\ \vdots & \vdots & & \vdots \\ f_1(y^{\omega*}) & f_2(y^{\omega*}) & \cdots & f_\omega(y^{\omega*}) \end{bmatrix}=\begin{bmatrix} V_1^* & V_1^{2*} & \cdots & V_1^{\omega*} \\ V_2^{1*} & V_2^* & \cdots & V_2^{\omega*} \\ \vdots & \vdots & & \vdots \\ V_\omega^{1*} & V_\omega^{2*} & \cdots & V_\omega^* \end{bmatrix} \tag{20}$$

β_q is calculated as:

$$\beta_q=\frac{\mu_q}{\left|V_q^*-\max\limits_{p=1,2,\dots,\omega}V_p^{q*}\right|} \tag{21}$$

where μ_q is the standard weight for the q^{th} objective. If μ_q is equal for all objectives, a longer distance between the utopia and nadir points results in a smaller β_q, indicating a lower weight of that objective.

The effect of the distance of nadir point from objective weights is considered in (21), enhancing decision-making accuracy. Figure 3 presents the schematic diagram of solving COS using weighted Chebyshev function. When μ_q is equal for all objectives, the COS is the intersection of the line connecting $\boldsymbol{a}$ and $\boldsymbol{r}$ with the Pareto frontier surface, representing the projection of $\boldsymbol{r}$ onto the Pareto frontier surface along the direction of $\boldsymbol{a}$, yielding the smallest weighted Chebyshev distance from the utopia point. Adjusting μ_q modifies the projection direction to obtain different COSs, e.g., the yellow and green points. Therefore, any COS can be found by minimizing the weighted Chebyshev function with an appropriate μ_q [29].

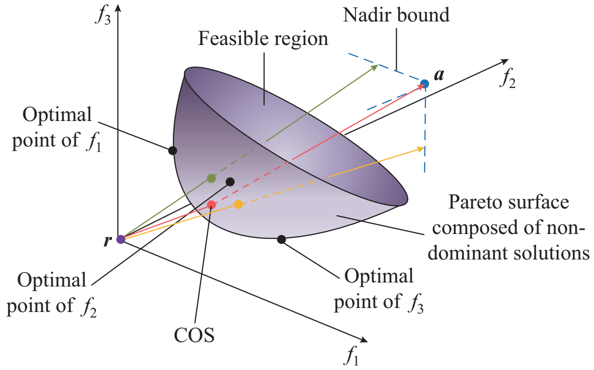

Fig. 3. Schematic diagram of solving COS using weighted Chebyshev function.

B. Multi-objective VF Matrix and Markov Decision Process (MDP)

Constructing VFs is essential for applying the ADP algorithm to solve multi-period stochastic optimization problems. A set of stochastic scenarios reflecting the uncertainties ($\Delta f_{\text{ag},t}$, $\Delta P_{\text{wp},t}$) is generated using the Latin hypercube sampling technique. By solving the deterministic optimization (DO) problem for each stochastic scenario, the VFs for each period can be obtained. In multi-objective multi-period stochastic optimization, VF matrices must be defined, extending the VFs from one-dimensional to multi-dimensional calculations [30]. The VF matrix $\boldsymbol{v}_t$ is geven as:

$$\begin{cases} \boldsymbol{v}_t=[\boldsymbol{V}_t^1,\boldsymbol{V}_t^2,\dots,\boldsymbol{V}_t^q,\dots,\boldsymbol{V}_t^\omega] \\ \boldsymbol{V}_t^q=[V_t^{1q},V_t^{2q},\dots,V_t^{pq},\dots,V_t^{\omega q}]^{\text{T}} \end{cases} \tag{22}$$

where the superscript pq denotes the value of the q^{th} objective function corresponding to the solution that minimizes the p^{th} objective function; and $\boldsymbol{V}_t^q$ is the q^{th} VF vector of $\boldsymbol{v}_t$.

Applying the ADP algorithm allows the multi-period MO-SOCDC model to be decomposed into multiple single-period

DO problems that can be addressed recursively. As shown in (23), the ADP-based integration with multi-objective optimization employs an extended Bellman equation derived from the optimality principle [23], where the second term on the right-hand side represents the expected value. $\boldsymbol{v}_{t+1}(\boldsymbol{S}_{t+1})|\boldsymbol{S}_t$ represents the conditional VF for the state $\boldsymbol{S}_{t+1}$ of the next period, incorporating how the current action $\boldsymbol{a}_t$ and state $\boldsymbol{S}_t$ influence the future states $\boldsymbol{S}_k$ for $k=t+1, t+2, \ldots, T$.

$$\begin{cases} \boldsymbol{v}_t(\boldsymbol{S}_t)=\min\limits_{\boldsymbol{a}_t}\left[\boldsymbol{C}_t(\boldsymbol{S}_t,\boldsymbol{a}_t)+\sum \Pr(\boldsymbol{w}_{t+1}|\boldsymbol{w}_t)\cdot(\boldsymbol{v}_{t+1}(\boldsymbol{S}_{t+1})|\boldsymbol{S}_t)\right] \\ \boldsymbol{S}_t=[\boldsymbol{R}_t,\boldsymbol{w}_t] \\ \boldsymbol{R}_t=[E_{\mathrm{h},t},E_{\mathrm{hy},t},E_{\mathrm{ag},t}] \\ \boldsymbol{w}_t=[P_{\mathrm{wp},t},f_{\mathrm{ag},t}] \\ \boldsymbol{a}_t=[\varphi_{\mathrm{hyi},t},\varphi_{\mathrm{hyo},t},\varphi_{\mathrm{hi},t},\varphi_{\mathrm{ho},t},f_{\mathrm{agi},t},f_{\mathrm{ago},t},P_{\mathrm{G},t},P_{\mathrm{DG},t},P_{\mathrm{mr},t},P_{\mathrm{cc},t}] \end{cases} \tag{23}$$

where $\Pr(\boldsymbol{w}_{t+1}|\boldsymbol{w}_t)$ is the transition probability function for stochastic quantities moving from $\boldsymbol{w}_t$ to $\boldsymbol{w}_{t+1}$; $\boldsymbol{C}_t(\boldsymbol{S}_t,\boldsymbol{a}_t)$ is the multi-objective cost matrix for $\boldsymbol{a}_t$; and $\boldsymbol{S}_t$ includes storage variables $\boldsymbol{R}_t$ and stochastic variables $\boldsymbol{w}_t$. To implement the MOADP algorithm, the MOSOCDC model is transformed into a multi-objective MDP (MMDP). The MMDP extends the traditional MDP [31] and is characterized by a four-element model $\{\boldsymbol{S}_t,\boldsymbol{a}_t,\boldsymbol{C}_t,\boldsymbol{T}_\mathrm{r}\}$, as shown in Fig. 4, where $\boldsymbol{T}_\mathrm{r}$ is the vector of state transition functions. In this MOSOCDC model, the state $\boldsymbol{S}_t$ includes storage capacity and stochastic variables. The optimization is performed by decoupling the periods, and the final optimal configured $\boldsymbol{E}_\Omega$ is determined as the maximum $\boldsymbol{E}_{\Omega,t}$ value across all periods. The obtained $\boldsymbol{E}_\Omega$ can meet the constraints across all periods despite stochastic fluctuations in $P_{\mathrm{wp},t}$ and $f_{\mathrm{ag},t}$. For instance, if the configured power is $P_{\mathrm{MR},t}$, the final optimal configured power is $P_\mathrm{MR}=\max\{P_{\mathrm{MR},1},P_{\mathrm{MR},2},\ldots,P_{\mathrm{MR},T}\}$. Additionally, the VF for the current period is derived from the instant cost of the current period and the VF of the next period. Since C_inv in f_1 is independent of t, it is necessary to adjust the VF calculations. Specifically, to align the VFs of the first period with f_1-f_3, the investment cost should be expressed as C_inv/T in $C_{1,t}(\boldsymbol{S}_t,\boldsymbol{a}_t)$ for VF calculations during each period.

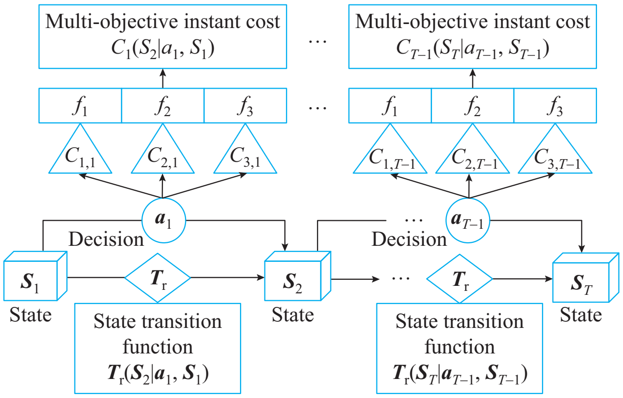

Fig. 4. MMDP.

Each column of $\boldsymbol{v}_t$ in (22) corresponds to the values of an optimization objective. Consequently, the multi-objective instant cost matrix can be expressed as in (24), with identical instant costs in each column. The values $C_{1,t}(\boldsymbol{S}_t,\boldsymbol{a}_t)$, $C_{2,t}(\boldsymbol{S}_t,\boldsymbol{a}_t)$, and $C_{3,t}(\boldsymbol{S}_t,\boldsymbol{a}_t)$ are calculated as given in (25)-(27). $\boldsymbol{T}_\mathrm{r}$ is shown in (28).

$$\boldsymbol{C}_t(\boldsymbol{S}_t,\boldsymbol{a}_t)=\begin{bmatrix} C_{1,t}(\boldsymbol{S}_t,\boldsymbol{a}_t) & C_{2,t}(\boldsymbol{S}_t,\boldsymbol{a}_t) & C_{3,t}(\boldsymbol{S}_t,\boldsymbol{a}_t) \\ C_{1,t}(\boldsymbol{S}_t,\boldsymbol{a}_t) & C_{2,t}(\boldsymbol{S}_t,\boldsymbol{a}_t) & C_{3,t}(\boldsymbol{S}_t,\boldsymbol{a}_t) \\ C_{1,t}(\boldsymbol{S}_t,\boldsymbol{a}_t) & C_{2,t}(\boldsymbol{S}_t,\boldsymbol{a}_t) & C_{3,t}(\boldsymbol{S}_t,\boldsymbol{a}_t) \end{bmatrix} \tag{24}$$

$$C_{1,t}(\boldsymbol{S}_t,\boldsymbol{a}_t)=C_\mathrm{inv}/T+C_{\mathrm{m},t}-C_{\mathrm{s},t} \tag{25}$$

$$C_{2,t}(\boldsymbol{S}_t,\boldsymbol{a}_t)=d_\mathrm{GB}f_{\mathrm{GB},t}+d_\mathrm{DG}P_{\mathrm{DG},t}+d_\mathrm{G}(1-\eta_t)\mu_\mathrm{G}P_{\mathrm{G},t} \tag{26}$$

$$C_{3,t}(\boldsymbol{S}_t,\boldsymbol{a}_t)=\sum_{i\in\Omega_\mathrm{w}}(P_{\mathrm{wp}i,t}-P_{\mathrm{w}i,t}) \tag{27}$$

$$\boldsymbol{R}_{t+1}=\boldsymbol{T}_\mathrm{r}(\boldsymbol{R}_t,\boldsymbol{a}_t,\boldsymbol{w}_t)=\boldsymbol{R}_t+E(\Delta\boldsymbol{R}_t(\boldsymbol{a}_t)|\boldsymbol{w}_t) \tag{28}$$

where $E(\cdot)$ denotes the expectation; and $C_{1,t}$, $C_{2,t}$, and $C_{3,t}$ are the elements of matrix $\boldsymbol{C}_t$.

C. MOADP Algorithm Based on Weighted Chebyshev Function

To address the low computational efficiency of traditional multi-objective optimization algorithms while accounting for stochastic fluctuations, an MOADP algorithm is proposed for solving the multi-period MOSOCDC problem. The MOADP algorithm leverages the extended Bellman equation to derive the analytical AVF expression for each period and objective. This allows the stochastic multi-period model to be decoupled into a series of single-period models, which are solved recursively. For solving the COS of each multi-objective single-period optimization problem, the weighted Chebyshev function is used, which quantifies the weighted Chebyshev distance between each AVF vector and the utopia point. The point with the smallest weighted Chebyshev distance in each period is selected as the COS for that period. Unlike the weighted sum method, which only considers the weights of individual objectives, the weighted Chebyshev function also considers the distance between the utopia and nadir points, providing a more comprehensive measure of optimization.

By traversing all periods through this process, the COS of the proposed MOSOCDC model can be efficiently obtained, significantly enhancing computational efficiency while ensuring accuracy.

1) Generation of Typical State Space and Sampling VF Vectors

To simplify the MOSOCDC calculation, a year is divided into three seasonal periods: summer, winter, and transitional season. Three representative days from three seasons are selected for the analysis. Utilizing the Latin hypercube sampling technique, stochastic scenarios are derived from the normal distributions of $P_{\mathrm{wp},t}$ and $f_{\mathrm{ag},t}$, distributed across seasons as $\alpha_\mathrm{s}/4$ for the winter scenarios, $\alpha_\mathrm{s}/4$ for the summer scenarios, and $\alpha_\mathrm{s}/2$ for the transitional period scenarios. The mean values are $P_{\mathrm{wp0},t}$ and $f_{\mathrm{ag0},t}$, while the standard deviations are $0.2P_{\mathrm{wp0},t}$ and $0.15f_{\mathrm{ag0},t}$. For each scenario of $\boldsymbol{w}_t$, a single-objective DO model is solved for each objective, resulting in α_s typical states and corresponding sampling VF matrices $\boldsymbol{v}_{t,j}$ ($t=1,2,\ldots,T$ and $j=1,2,\ldots,\alpha_\mathrm{s}$) for the three objectives, where the q^th vector is $\boldsymbol{V}_{t,j}^q=[V_{t,j}^{1q},V_{t,j}^{2q},V_{t,j}^{3q}]^\mathrm{T}$ and $q=$

1, 2, 3. Additionally, the corresponding sampling instant costs before normalization $\hat{C}^{pq}_{t,j}(\boldsymbol{S}_{t,j}, \boldsymbol{a}_t)$ ($p=1,2,3$) are obtained by solving the DO model for each period, objective, and typical state. These sampling instant costs must then be normalized as:

$$\begin{cases} C^{pq}_{t,j}(\boldsymbol{S}_{t,j}, \boldsymbol{a}_t) = \dfrac{\hat{C}^{pq}_{t,j}(\boldsymbol{S}_{t,j}, \boldsymbol{a}_t) - f_{q,t\min}}{f_{q,t\max} - f_{q,t\min}} \\ f_{q,t\max} = \max\limits_{\substack{p=1,2,3 \\ j=1,2,\ldots,\alpha_{\mathrm{s}}}} \hat{C}^{pq}_{t,j}(\boldsymbol{S}_{t,j}, \boldsymbol{a}_t) \\ f_{q,t\min} = \min\limits_{\substack{p=1,2,3 \\ j=1,2,\ldots,\alpha_{\mathrm{s}}}} \hat{C}^{pq}_{t,j}(\boldsymbol{S}_{t,j}, \boldsymbol{a}_t) \end{cases} \tag{29}$$

where $f_{q,t\max}$ and $f_{q,t\min}$ are the maximum and minimum instant cost values for the q^{th} objective within the typical state space, respectively. All terms related to the optimization objectives in (30), (31), and (33)-(36) are expressed as normalized values.

The transition probability of $\Pr(\boldsymbol{w}_{t+1}|\boldsymbol{w}_t)$ can be derived from historical data using the method in [24]. $P_{\mathrm{wp},t}$ and $f_{\mathrm{ag},t}$ are divided into N_{w} and N_{ag} intervals, respectively, for analysis.

2) Computation of Analytical Expressions of AVF Under Three Objectives

The Bellman equation for solving the single-objective stochastic OCDC model by transforming it into the single-objective single-period optimization model is given in (30), in which the number of divided intervals of stochastic variables is $N_{\mathrm{e}} = N_{\mathrm{w}} N_{\mathrm{ag}}$ [24]. The AVF for time period t is obtained by minimizing the weighted sum of the instant cost during time period t and the AVF for time period $t+1$ i, i.e., $\bar{V}^{pq}_{t+1}(\boldsymbol{S}_{t+1})$.

$$V^{pq}_{t,j}(\boldsymbol{S}_{t,j}) = \begin{cases} \min\left\{ C^{pq}_{t,j}(\boldsymbol{S}_{t,j}, \boldsymbol{a}_t) + \sum\limits_{n=1}^{N_{\mathrm{e}}} \Pr(\boldsymbol{w}_{t+1,n}|\boldsymbol{w}_t) \bar{V}^{pq}_{t+1}(\boldsymbol{S}_{t+1}) \right\} \\ \text{s.t. } (7)\text{-}(17) \end{cases} \tag{30}$$

To compute the AVFs corresponding to the α_{s} typical states for the three objectives, AVFs are determined through a backward recursive process starting from the final period and moving toward the first, by utilizing the analytical expressions of the AVFs for the subsequent period. By solving (30), α_{s} sets of $\boldsymbol{S}_{t,j} - V^{pq}_{t,j}(\boldsymbol{S}_{t,j})$ samples are obtained. The least squares method is applied to fit the data using a cubic polynomial as the fitting function, as shown in (31). The coefficients $\boldsymbol{A}_{t+1}$, $\boldsymbol{B}_{t+1}$, $\boldsymbol{c}_{t+1}$, e_{t+1} are determined by minimizing the fitting residuals, as shown in (32). Assume that elements in $\boldsymbol{S}_{t+1}$ are $S_1, S_2, \ldots, S_n$, and the expression of $\boldsymbol{S}'_{t+1}$ can refer to [23].

$$\bar{V}^{pq}_{t+1}(\boldsymbol{S}_{t+1}) = \frac{1}{6}\boldsymbol{S}'_{t+1}\boldsymbol{A}_{t+1}\boldsymbol{S}_{t+1} + \frac{1}{2}\boldsymbol{S}^{\mathrm{T}}_{t+1}\boldsymbol{B}_{t+1}\boldsymbol{S}_{t+1} + \boldsymbol{c}^{\mathrm{T}}_{t+1}\boldsymbol{S}_{t+1} + e_{t+1} \tag{31}$$

$$\arg \min_{\substack{\boldsymbol{A}_{t+1}, \boldsymbol{B}_{t+1}, \\ \boldsymbol{c}_{t+1}, e_{t+1}}} \sum_{j=1}^{\lambda_s} \left\| \bar{V}^{pq}_{t+1,j}(\boldsymbol{A}_{t+1}, \boldsymbol{B}_{t+1}, \boldsymbol{c}_{t+1}, e_{t+1}, \boldsymbol{S}_{t+1,j}) - V^{pq}_{t+1,j} \right\| \tag{32}$$

The computation of AVFs starts by assigning the sampling VFs to the α_{s} typical states in the final time period T. Subsequently, the analytical expressions of AVFs are derived using (31) and (32). To simplify the process, the midpoints of N_{e} divided intervals of $\boldsymbol{w}_{T,n}$ for $n=1,2,\ldots,N_{\mathrm{e}}$ are substituted into $\Pr(\boldsymbol{w}_{T,n}|\boldsymbol{w}_{T-1})$. By minimizing (30), the corresponding AVFs $V^{pq}_{T-1,j}(\boldsymbol{S}_{T-1,j})$ are derived. This method continues recursively through periods $T-1$, $T-2$, etc., back to time period 1. For a three-objective optimization problem, (30) is solved nine times per period. The result provides the AVF matrices for α_{s} typical states and the analytical AVF expressions for each objective across all periods ($p=1,2,3$, $q=1,2,3$, and $t=1,2,\ldots,T$).

3) Solution of COS and Optimal Configuration Scheme

Once the analytical AVF expressions for each period are obtained, the multi-objective single-period optimization model (33) is solved, which provides the COS along with the corresponding optimal configuration scheme.

$$\begin{cases} \boldsymbol{a}_t = \arg \min\limits_{\boldsymbol{a}_t} \left\{ C_{\mathrm{ct}}(\boldsymbol{S}_t, \boldsymbol{a}_t) + \sum\limits_{n=1}^{N_{\mathrm{e}}} \Pr(\boldsymbol{w}_{t+1,n}|\boldsymbol{w}_t) d_{t+1}(\boldsymbol{S}_{t+1}) \right\} \\ \text{s.t. } (7)\text{-}(17) \end{cases} \tag{33}$$

Through the weighted Chebyshev calculation in Supplementary Material A, the optimization problem in (33) is converted into a min-max bi-level optimization problem with both decision variables $\boldsymbol{a}_t$. The auxiliary variable ϕ is introduced to simplify (33) into a single-layer minimization problem, as shown in (34).

$$\begin{cases} \boldsymbol{a}_t = \arg \min\limits_{\boldsymbol{a}_t} C_{ct}(\boldsymbol{S}_t, \boldsymbol{a}_t) \sum\limits_{n=1}^{N_{\mathrm{e}}} \Pr(\boldsymbol{w}_{t+1,n}|\boldsymbol{w}_t) \phi \\ \text{s.t. } \phi \ge \dfrac{1}{3} \dfrac{|\boldsymbol{r} - \boldsymbol{V}^1_{t+1}(\boldsymbol{S}_{t+1})|}{|\bar{V}^{11}_{t+1}(\boldsymbol{S}_{t+1}) - \bar{V}^{1q'}_{t+1}(\boldsymbol{S}_{t+1})|} \\ \qquad \phi \ge \dfrac{1}{3} \dfrac{|\boldsymbol{r} - \boldsymbol{V}^2_{t+1}(\boldsymbol{S}_{t+1})|}{|\bar{V}^{22}_{t+1}(\boldsymbol{S}_{t+1}) - \bar{V}^{2q''}_{t+1}(\boldsymbol{S}_{t+1})|} \\ \qquad \phi \ge \dfrac{1}{3} \dfrac{|\boldsymbol{r} - \boldsymbol{V}^3_{t+1}(\boldsymbol{S}_{t+1})|}{|\bar{V}^{33}_{t+1}(\boldsymbol{S}_{t+1}) - \bar{V}^{3q'''}_{t+1}(\boldsymbol{S}_{t+1})|} \\ \qquad (7)\text{-}(17) \end{cases} \tag{34}$$

Finally, the optimal decision $\boldsymbol{a}_t$ is determined by solving the optimization problem in (34) from the first period to the last. The detailed calculation steps are as follows.

Step 1: initialize $\boldsymbol{S}_t$ and set each component in $\boldsymbol{R}_1$ to be half of the total storage quantity, so for $t=1$, $\boldsymbol{S}_t = \boldsymbol{S}_1(\boldsymbol{R}_1, \boldsymbol{w}_1)$.

Step 2: assume the current time period is t; compare the results of AVF calculations numerically to determine the objectives q', q'', and q''' (q', q'', and q''' can be 1, 2, or 3) that maximize the values of $\bar{V}^{1q}_{t+1}(\boldsymbol{S}_{t+1})$, $\bar{V}^{2q}_{t+1}(\boldsymbol{S}_{t+1})$, and $\bar{V}^{3q}_{t+1}(\boldsymbol{S}_{t+1})$, respectively; and substitute them into (34).

Step 3: substitute the midpoints of N_{e} divided intervals of $\boldsymbol{w}_{t+1,n}$ ($n=1,2,\ldots,N_{\mathrm{e}}$), the analytical AVF expression $\bar{V}^{pq}_{t+1}(\boldsymbol{S}_{t+1})$ ($p=1,2,3$ and $q=1,2,3$), and $\boldsymbol{R}_t$ from the previous period into (34), and minimize the optimization model in (34) to obtain $\boldsymbol{a}_t$ and $\boldsymbol{C}_t(\boldsymbol{S}_t, \boldsymbol{a}_t)$ for the current time period.

Step 4: increase $t=t+1$ and repeat *Steps 2* and *3* until all periods are processed. Determine the optimal configuration scheme, i.e., the optimal values of the components in $\boldsymbol{E}_{\Omega}$ using the solution method outlined in Section III-B.

IV. CASE STUDY

Figure 5 illustrates the wiring diagram of an actual OO-IES. The OGPP and OWF are positioned in the South China Sea, whereas the GCHPP is positioned in Zhongshan City, China. The power network consists of 17 buses, both the heat and gas networks include nine nodes, and the OGPP has three gas wells. Each wind turbine has an installed capacity of 5.5 MW. The year is divided into 365 days, with 178 days in the transitional season, 95 days in summer, and 92 days in winter. The divided intervals are set with $N_{ag}=5$ and $N_w=5$. Power, heat, gas, and hydrogen load curves for 3 typical days are illustrated in Supplementary Material A Fig. SA1. The forecasted $f_{ag,t}$ and $P_{wp,t}$ on these days are shown in Supplementary Mterial A Figs. SA2. Investment and maintenance costs for CC-P2G, along with other system parameters, are detailed in Supplementary Mterial A Tables SAI and SAII, respectively. All simulations are conducted on a computer equipped with an Intel$^{(R)}$ Xeon$^{(R)}$ E3-1270 CPU @ 3.60 GHz and 32 GB of RAM, utilizing MATLAB R2019a and GAMS win64 24.5.3. The SBB solver is employed to handle the single-period DO problems formulated in (30) and (34).

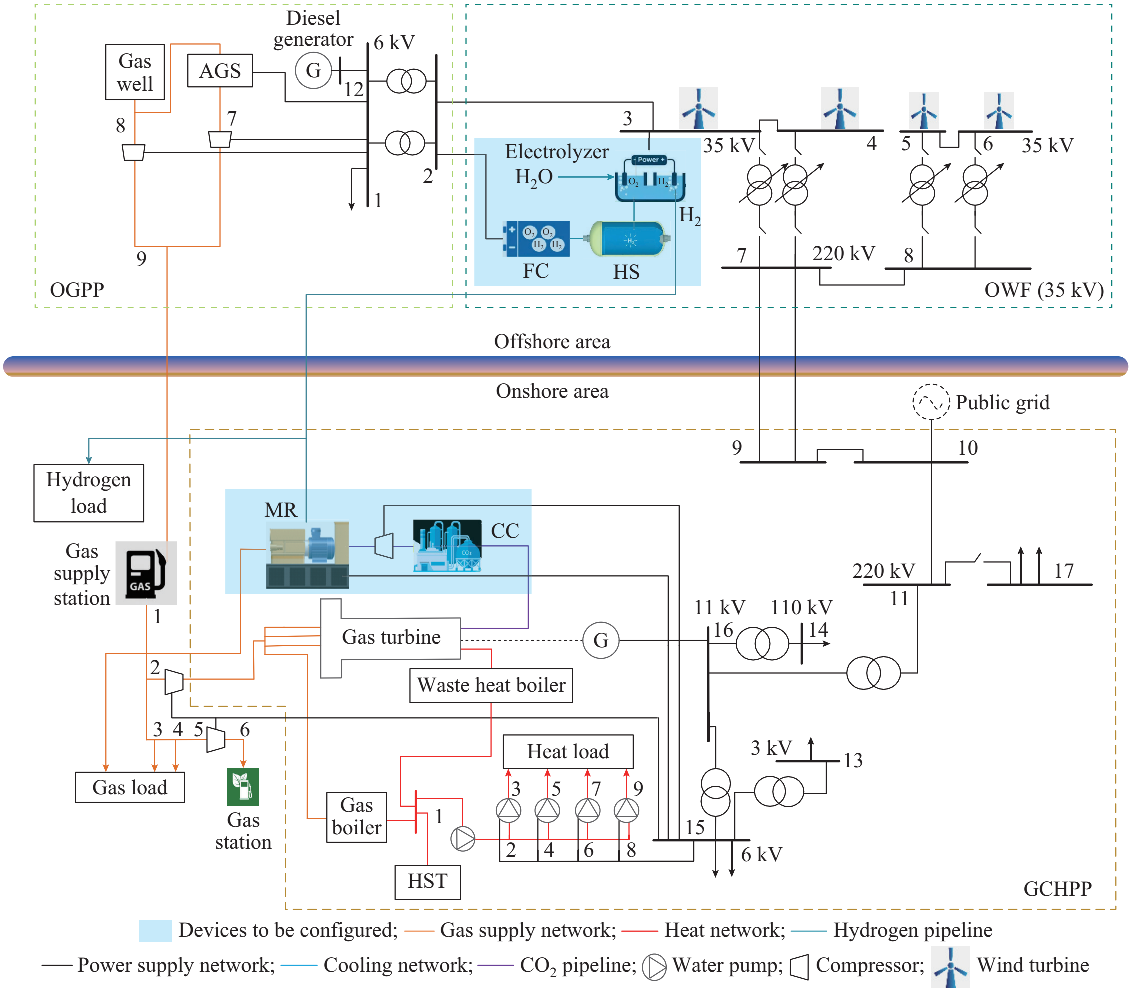

Fig. 5. Wiring diagram of an actual OOIES.

A. Analysis of Multi-objective Optimization Results

1) AVF Matrix Under Three Objectives

$\alpha_s=40$ stochastic scenarios (including three typical forecasting scenarios) are generated using the Latin hypercube sampling method. The 40 sampled scenarios for total OWF power output and mass flow rates of gas wells are displayed in Supplementary Mterial A Fig. SA3. By solving (30) recursively from the last period to the first, the AVFs for each period are computed. These calculations produce normalized AVF matrices corresponding α_s to the 40 typical states during each period, as illustrated in Fig. 6, where colored marks respresent different stochastic scenarios. Moreover, the results indicate that when optimizing a single objective p, the AVF for that objective p is obviously smaller than those for optimizing the other two objectives. This phenomenon occurs due to SOO focusing exclusively on the selected objective while neglecting the optimization of the other objectives.

2) Computation Results of Multi-objective Optimization

The ADP algorithm from [23] is used to determine the OCDC results for the three SOO models with objectives in (2)-(4). By using Chebyshev standard weights as $\mu_1=\mu_2=\mu_3=1/3$, the OCDC results for the proposed MOSOCDC model are obtained and presented in Table II.

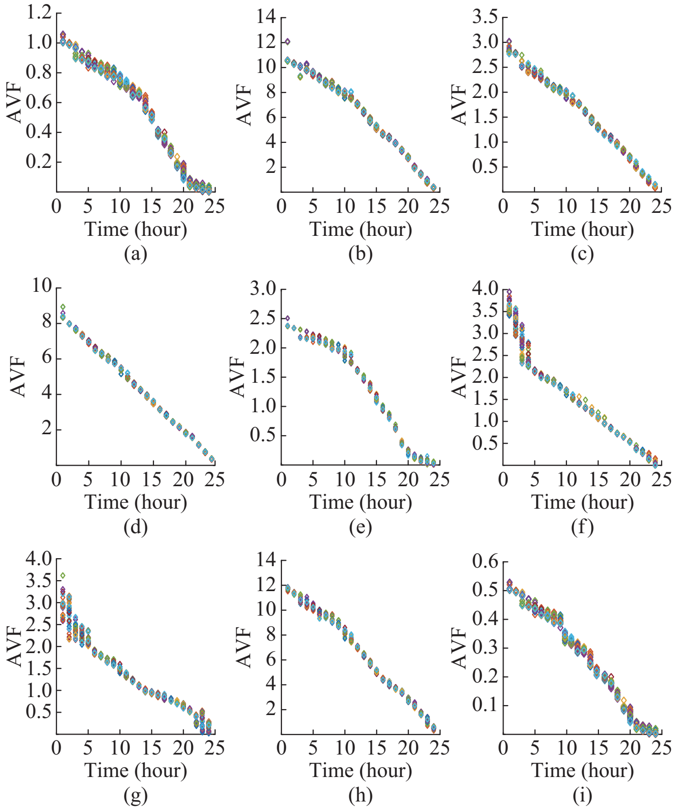

Fig. 6. AVF matrices of typical states during each period. (a) V_{11}. (b) V_{12}. (c) V_{13}. (d) V_{21}. (e) V_{22}. (f) V_{23}. (g) V_{31}. (h) V_{32}. (i) V_{33}.

The OCDC results for each SOO model differ, reflecting the conflict among the three objectives. Specifically, objective 1 focuses on economic efficiency and yields smaller configured device capacities due to the proportional relationship between investment costs and device capacities. In contrast, objectives 2 and 3 yield larger configured device capacities, as increasing the device capacities in CC-P2G helps reduce carbon emissions and wind power curtailment. A comparison between SOO and MOO results is provided in Table III.

The results indicate that when minimizing the total costs, the obtained carbon emissions increase due to less configured device capacities in CC-P2G. When the carbon emissions are minimized, the obtained total costs are higher because OOIES requires greater configured device capacities in CC-P2G. When minimizing the wind curtailment, the obtained total costs rise because OOIES needs additional system flexibility to balance the wind power fluctuation, further increasing the system operation costs. The weighted Chebyshev distance of the MOO model is the smallest, indicating that it is closer to the utopia point than the three SOO models. Therefore, the COS of the MOO model demonstrates a higher degree of comprehensive optimization than the individual SOO models.

In the proposed MOSOCDC model, by initially setting the Chebyshev standard weights to $\mu=\mu_2=\mu_3=1/3$ and adjusting them to values $\mu_1=\{0, 1/6, 2/6, \ldots, 1\}$, $\mu_2=\{0, 1/6, 2/6, \ldots, 1-\mu_1\}$, and $\mu_3=1-\mu_1-\mu_2$, 49 POSs are obtained for each combination of weight values.

TABLE II

Single-objective and Multi-objective Optimal Configuration Results

Objective	Device	Device capacity configuration (MW/MWh)	Average daily investment cost (¥)
min f_1	EC	12.84	1528.728
	HS	31.54	6823.451
	FC	14.34	1728.564
	MR	4.80	12828.586
	CC	9.14	18261.649
min f_2	EC	31.76	2528.208
	HS	52.53	8154.918
	FC	25.42	2707.846
	MR	11.34	23791.455
	CC	15.48	26846.945
min f_3	EC	27.64	2264.646
	HS	56.84	8754.618
	FC	32.61	3597.025
	MR	12.65	26151.090
	CC	15.64	27136.949
MOO	EC	23.51	1871.479
	HS	39.15	7131.071
	FC	16.47	2037.716
	MR	6.48	14581.625
	CC	13.62	21561.005

TABLE III

Single-objective and Multi-objective Optimization Results

Solution	f_1 (¥)	f_2 (t)	f_3 (MWh)	Chebyshev distance
min f_1	100482.607	54.710	16.582	1.018
min f_2	172180.481	19.930	22.420	1.239
min f_3	180147.251	63.093	1.564	1.324
COS	127851.652	40.933	6.568	0.948

The corresponding Pareto frontier using weighted Chebyshev function is plotted in Fig. 7. The red point on the plot represents the COS, which is closest to the utopia point with standard weights μ_1, μ_2, and μ_3 being 1/3, 1/2, and 1/6, respectively. The purple points indicate other POSs obtained through the proposed MOADP algorithm. The COS is nearer to the utopia point than the other POSs.

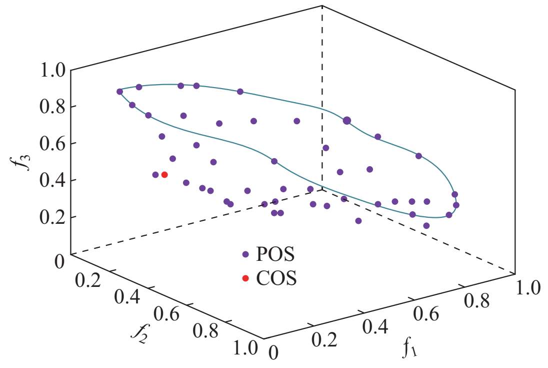

Fig. 7. Pareto frontier using weighted Chebyshev function.

3) Analysis of MOSOCDC Model

To assess the necessity of configuring CC-P2G devices in the OOIES, the MOSOCDC model is solved using the proposed MOADP algorithm, and the solution results are compared with the optimal results of the case excluding CC-P2G devices. The optimization model of this case does not include C_{inv} and C_{m} in the objective functions, and the CC-P2G related constraints in (11)-(14) and the second formula of (10) are excluded. In this scenario, only the ECs of CC-P2G are used to supply hydrogen loads, and the results are presented in Table IV. The optimal configuration for CC-P2G devices increases f_1 by 14.47% compared with the unconfigured method. However, the proposed MOSOCDC model significantly reduces f_2 and f_3 by 69.68% and 81.73%, respectively. Therefore, configuring CC-P2G devices increases energy utilization, lowers carbon emissions, and improves the operation flexibility of the OOIES in coordinating multiple energy operations.

TABLE IV
COMPARISON OF RESULTS OF UNCONFIGURED AND CONFIGURED CC-P2G DEVICES

CC-P2G device	C_{inv} (¥)	f_1 (¥)	f_2 (t)	f_3 (MWh)
Unconfigured		111686.349	135.024	35.944
Configured	49803.160	127851.652	40.933	6.568

The configured CC-P2G devices enable energy conversion among electricity, hydrogen, and gas. To analyze the relationship between the configured device capacities in CC-P2G and energy prices, it is assumed that the gas price varies from 2 to 3.8 ¥/(N·m^3) and the hydrogen price varies from 3.3 to 6.3 ¥/(N·m^3). As the gas price rises to 3.0 ¥/(N·m^3), profits from gas sales increase, driving a significant boost in configured device capacities. Beyond this price unit, further increases in configured device capacities become uneconomical. As the hydrogen price rises between 3.3 and 5.1 ¥/(N·m^3), the configured device capacities increase, enhancing economic returns. However, when the hydrogen price reaches 5.1-6.3 ¥/(N·m^3), the configured device capacities remain relatively stable. This outcome is observed because the gas price significantly influences the profitability of SNG produced by the MR. For other devices, particularly ECs involved in hydrogen production, increasing the configured device capacities boosts the profitability of hydrogen sales. However, the associated investment costs rise alongside the increase of device capacities, leading to minimal changes in device capacities when the prices surpass certain thresholds.

B. Energy and Carbon Dispatch Under OCDC in CC-P2G

On a representative summer day, OCDC in CC-P2G linked to the COS is input into the proposed MOSOCDC model to derive the optimal dispatch strategy for the OOIES. Figure 9(a) illustrates the power dispatch scheme. The OWF output meets the power demand for the OGPP, while any shortfall is supplemented by the DG and FC. During low-demand periods, the EC converts power into hydrogen, which helps to increase renewable energy usage.

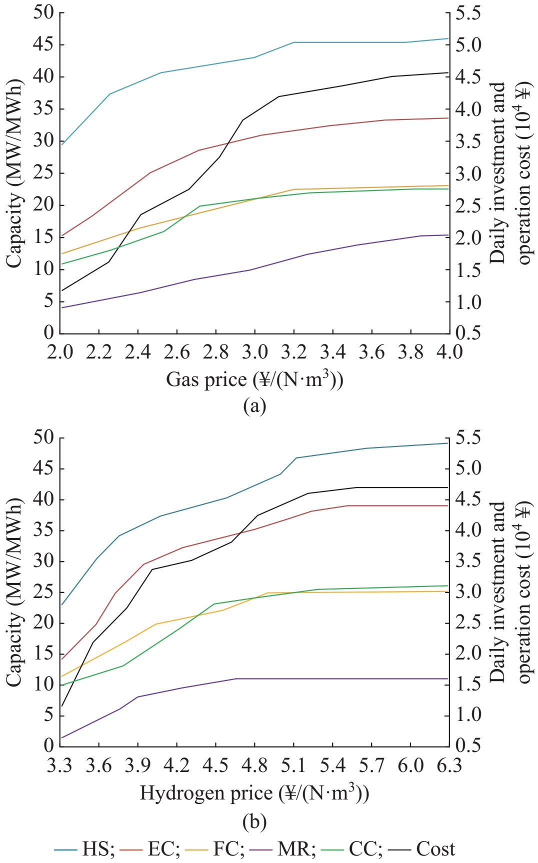

Fig. 8. Influence of gas and hydrogen prices on configured device capacities. (a) Gas price. (b) Hydrogen price.

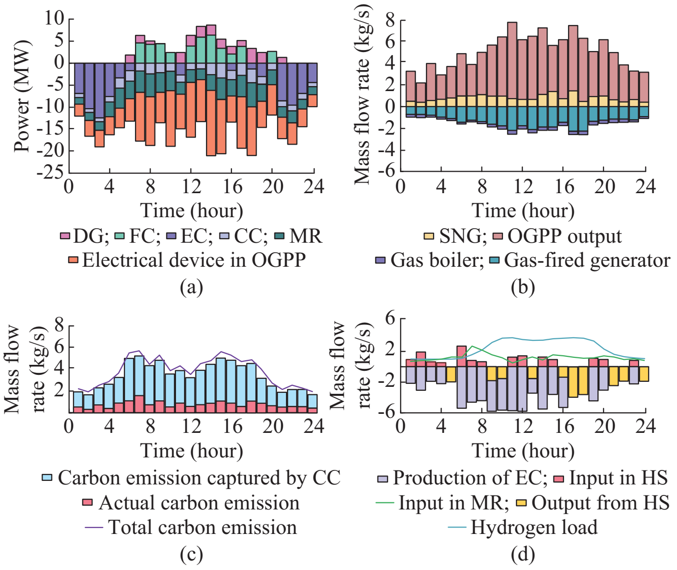

Fig. 9. Optimal dispatch scheme of a typical summer day. (a) Power dispatch scheme. (b) Gas dispatch scheme. (c) CO$_2$ dispatch scheme. (d) Hydrogen dispatch scheme.

The amount of SNG produced by the MR is directly linked to the CO$_2$ captured by the CC, resulting in a positive correlation between the CC and MR power consumption. Figure 9(b) shows the gas dispatch scheme, where the gas supply of OOIES mainly consists of the extracted gas from OGPP and the SNG. The MR produces 865.94 t of SNG in the 1-day cycle. Figure 9(c) reveals that the CC captures 74.89% of the total CO_2 emissions from gas-fired generators. Lastly, Fig. 9(d) demonstrates that hydrogen demand is met by the EC during production periods, while the stored hydrogen satisfies hydrogen demand during other time periods.

Based on the analysis above, the processes of hydrogen production via water electrolysis, power generation through the FC, CC by MR, and gas storage demonstrate the system ability to facilitate energy conversion and transfer. Excess energy is converted and redirected to meet various energy demands through conversion devices. For instance, surplus wind power is fed into the EC, where it is converted into SNG to supply gas loads. This collaborative optimization strategy effectively reduces CO_2 emissions and increases the accommodation of renewable energy, validating the efficacy of the obtained OCDC in CC-P2G through the proposed algorithm.

C. Comparison of Different MOSO Algorithms

In traditional algorithms for solving MOSO problems, the weighted sum method is commonly used to transform an MOO problem into SOO problem, and the scenario algorithm is typically used to convert stochastic optimization problems into DO problems. As shown in Table V, the proposed MOADP algorithm demonstrates improved computational efficiency. In the weighted sum algorithm, 10 discrete points are selected within [0,1] for the weight of each objective, generating a POS set from which the COS is chosen. Table V highlights the low computational efficiency of the scenario algorithm, where the computational time grows as the number of scenarios α_s increases.

TABLE V
COMPARATIVE RESULTS OF FOUR DIFFERENT MOSO ALGORITHMS

Algorithm	α_s	f_1 (¥)	f_2 (t)	f_3 (MWh)	Computational time (s)
Weighted sum + scenario	40	128158.419	41.531	6.754	4788.067
	60	128358.643	41.519	6.743	8592.946
	80				Overflow
Chebyshev function + scenario	40	127989.117	40.967	6.590	3986.584
	60	127958.594	40.959	6.711	6568.620
	80				Overflow
Weighted sum + ADP	40	128096.240	41.397	6.723	1325.629
	60	127984.151	41.329	6.748	2487.013
	80	128016.045	41.286	6.737	3629.177
Chebyshev function + ADP	40	127851.652	40.933	6.568	869.640
	60	127782.260	40.919	6.610	1129.541
	80	127755.484	41.055	6.526	1640.694

Similarly, the weighted sum algorithm suffers from inefficiency, as it requires calculating numerous discrete POSs before determining the COS. When $\alpha_s = 40$, the proposed MOADP algorithm reduces computational time by 81.84%, 78.19%, and 34.40% compared with the other three algorithms. When $\alpha_s = 60$, time is reduced by 86.86%, 82.81%, and 54.58%. When $\alpha_s = 80$, the weighted sum + scenario and Chebyshev function + scenario algorithms experience RAM overflow due to the large scenario scale, preventing optimization results. Compared with the weighted sum + ADP algorithm, the proposed MOADP algorithm reduces computational time by 54.79%. These results demonstrate the superior computational efficiency of the proposed MOADP algorithm based on the weighted Chebyshev function.

The quality of the optimal solutions is higher in the multi-objective optimization algorithm based on the weighted Chebyshev function, as its COS values for each objective are smaller than those obtained using the weighted sum algorithm. This phenomenon occurs because the weighted Chebyshev function considers the COS distance from both the utopia and nadir points, resulting in a more optimal COS. In contrast, the weighted sum algorithm often produces an uneven distribution of POSs in the obtained Pareto frontier, which can result in a less desirable COS. Therefore, the proposed algorithm demonstrates a clear advantage in producing high-quality COS outcomes.

V. CONCLUSION

An MOSO algorithm for optimizing the device capacities in CC-P2G of OOIES is introduced, accounting for the stochastic fluctuations in OWF power and AG output. A case study on an actual OOIES validates the effectiveness and efficiency of the proposed MOADP algorithm. The OCDC in CC-P2G obtained from the proposed MOSODCD model increases the total cost by 14.47% but reduces carbon emissions by 69.68% and wind power curtailment by 81.73% compared with the optimal operation of the system before configuration. By incorporating the effect of the solution distance from the nadir point on the objective weights, the MOADP algorithm achieves a COS with a high degree of comprehensive optimization across all objectives. Additionally, the MOADP algorithm reduces CPU time by more than 34.40% compared with other MOSO algorithms, which significantly boosts computational efficiency in solving MOSO problems.

This study introduces the MOADP algorithm to address the three-objective optimization problem for the OCDC in CC-P2G of OOIES. Future work will explore extending this algorithm to handle MOSO problems involving more than three objectives, particularly when factoring in objectives such as the secure and reliable operation of OOIES under contingencies.

REFERENCES

[1] K. Sun, H. Zhou, W. Yao *et al.*, "Comprehensive control of MMC-HVDC integrated offshore wind farm system including optimized energy control for fast frequency support," *Journal of Modern Power Systems and Clean Energy*, vol. 13, no. 6, pp. 1966-1979, Dec. 2025.

[2] X. Sheng, S. Lin, W. Liang *et al.*, "Optimal long-term planning of CCUS and carbon trading mechanism in offshore-onshore integrated energy system," *Applied Energy*, vol. 379, p. 124983, Feb. 2025.

[3] X. Liu, "Research on optimal placement of low-carbon equipment capacity in integrated energy system considering carbon emission and carbon trading," *International Journal of Energy Research*, vol. 46, no. 15, pp. 20535-20555, Nov. 2022.

[4] H. Hou, T. Xu, X. Wu *et al.*, "Optimal capacity configuration of the wind-photovoltaic-storage hybrid power system based on gravity energy storage system," *Applied Energy*, vol. 271, p. 115502, Aug. 2020.

[5] Y. Qiao, F. Hu, W. Xiong *et al.*, "Multi-objective optimization of inte-

grated energy system considering installation configuration," *Energy*, vol. 263, p. 125785, Jan. 2023.

[6] H. Shen, H. Zhang, Y. Xu *et al.*, "Multi-objective capacity configuration optimization of an integrated energy system considering economy and environment with harvest heat," *Energy Conversion and Management*, vol. 269, p. 116116, Oct. 2022.

[7] Y. Dong, C. Wang, H. Zhang *et al.*, "A novel multi-objective optimization framework for optimal integrated energy system planning with demand response under multiple uncertainties," *Information Sciences*, vol. 663, p. 120252, Mar. 2024.

[8] J. Zou, X. Yang, Z. Liu *et al.*, "Multi-objective bi-level optimization algorithm based on preference selection to solve energy hub system planning problems," *Energy*, vol. 232, p. 120995, Oct. 2021.

[9] J. Zheng, Y. Kou, M. Li *et al.*, "Stochastic optimization of cost-risk for integrated energy system considering wind and solar power correlated," *Journal of Modern Power Systems and Clean Energy*, vol. 7, no. 4, pp. 1472-1483, Jul. 2019.

[10] H. Chen, L. Gao, and Z. Zhang, "Multi-objective optimal scheduling of a microgrid with uncertainties of renewable power generation considering user satisfaction," *International Journal of Electrical Power & Energy Systems*, vol. 131, p. 107142, Oct. 2021.

[11] F. Wei, Q. Wu, Z. Jing *et al.*, "Optimal unit sizing for small-scale integrated energy systems using multi-objective interval optimization and evidential reasoning approach," *Energy*, vol. 111, p. 933-946, Sept. 2016.

[12] M. Qin, Y. Yang, X. Zhao *et al.*, "Low-carbon economic multi-objective dispatch of integrated energy system considering the price fluctuation of natural gas and carbon emission accounting," *Protection and Control of Modern Power Systems*, vol. 8, no. 4, pp. 1-18, Oct. 2023.

[13] Y. Dong, H. Zhang, C. Wang *et al.*, "Robust optimal scheduling for integrated energy systems based on multi-objective confidence gap decision theory," *Expert Systems with Applications*, vol. 228, p. 120304, Oct. 2023.

[14] R. Yan, J. Wang, S. Lu *et al.*, "Multi-objective two-stage adaptive robust planning method for an integrated energy system considering load uncertainty," *Energy and Buildings*, vol. 235, p. 110741, Mar. 2021.

[15] X. Chen, W. Dong, L. Yang *et al.*, "Scenario-based robust capacity planning of regional integrated energy systems considering carbon emissions," *Renewable Energy*, vol. 207, pp. 359-375, May 2023.

[16] J. Si, A. G. Barto, W. B. Powell *et al.*, "Applications of approximate dynamic programming in power systems control," in *Handbook of Learning and Approximate Dynamic Programming*. New York: IEEE, 2004, pp. 479-515.

[17] W. B. Powell and S. Meisel, "Tutorial on stochastic optimization in energy – Part I: modeling and policies," *IEEE Transactions on Power Systems*, vol. 31, no. 2, pp. 1459-1467, Mar. 2016.

[18] R. E. Bellman, "The optimal inventory equation," in *Dynamic Programming*. Princeton: Princeton University Press, 2010, pp. 152-183.

[19] W. Liang, S. Lin, M. Liu *et al.*, "Stochastic economic dispatch of regional integrated energy system considering the pipeline dynamics using improved approximate dynamic programming," *International Journal of Electrical Power & Energy Systems*, vol. 141, p. 108190, Oct. 2022.

[20] Y. Zhang, P. Sun, X. Ji *et al.*, "Low-carbon economic dispatch of integrated energy systems considering extended carbon emission flow," *Journal of Modern Power Systems and Clean Energy*, vol. 12, no. 6, pp. 1798-1809, Nov. 2024.

[21] X. Xue, X. Ai, J. Fang *et al.*, "Real-time schedule of integrated heat and power system: a multi-dimensional stochastic approximate dynamic programming approach," *International Journal of Energy Research*, vol. 134, no. 15, p. 107427, Jan. 2022.

[22] S. Mei, Q. Tan, A. Trivedi *et al.*, "A two-step optimization model for virtual power plant participating in spot market based on energy storage power distribution considering comprehensive forecasting error of renewable energy output," *Applied Energy*, vol. 376, p. 124234, Dec. 2024.

[23] Y. Pan, S. Lin, W. Liang *et al.*, "Stochastic optimal dispatch of offshore-onshore regional integrated energy system based on improved state-space approximate dynamic programming," *International Journal of Electrical Power & Energy Systems*, vol. 155, p. 109661, Jan. 2024.

[24] S. Lin, Y. Wang, M. Liu *et al.*, "Stochastic optimal dispatch of PV/wind/diesel/battery microgrids using state-space approximate dynamic programming," *IET Generation Transmission & Distribution*, vol. 13, no. 15, pp. 3195-3500, Aug. 2019.

[25] Y. Qiu, Q. Li, Y. Ai *et al.*, "Two-stage distributionally robust optimization-based coordinated scheduling of integrated energy system with electricity-hydrogen hybrid energy storage," *Protection and Control of Modern Power Systems*, vol. 8, no. 2, pp. 542-555, Jul. 2023.

[26] M. Talaie, F. Jabari, and A. A. Foroud, "Modeling and economic dispatch of a novel fresh water, methane and electricity generation system considering green hydrogenation and carbon capture," *Energy Conversion and Management*, vol. 302, p. 118087, Feb. 2024.

[27] J. Yang, N. Zhang, C. Kang *et al.*, "A state-independent linear power flow model with accurate estimation of voltage magnitude," *IEEE Transactions on Power Systems*, vol. 32, no. 5, pp. 3607-3617, Sept. 2017.

[28] J. Yu, D. Yang, J. Cao *et al.*, "Robust state estimation for an electricity-gas-heat integrated energy system considering dynamic characteristics," *Protection and Control of Modern Power Systems*, vol. 9, no. 1, pp. 65-80, Jan. 2024.

[29] X. Liu, J. Wu, N. Jenkins *et al.*, "Combined analysis of electricity and heat networks," *Applied Energy*, vol. 162, pp. 1238-1250, Aug. 2020.

[30] P. Perny and P. Weng, "On finding compromise solutions in multiobjective Markov decision processes," in *Proceedings of European Conference on Artificial Intelligence*, Amsterdam, Netherlands, Aug. 2010, pp. 969-970.

[31] L. Galand and P. Perny, "Search for compromise solutions in multi-objective state space graphs," *Proceedings of ECAI*, Riva del Garda, Italy, May 2006, pp. 93-97.

Shunjiang Lin received the B.S. degree from the South China University of Technology, Guangzhou, China, in 2003, and the Ph.D. degree from Hunan University, Changsha, China, in 2008, both in electrical engineering. He is currently the Professor with the School of Electric Power Engineering, South China University of Technology. His research interests include optimal operation and control of power systems and integrated energy systems.

Xuan Sheng received the B. S. degree in electrical engineering from the South China University of Technology, Guangzhou, China, in 2022, where he is currently pursuing the Ph.D. degree. His research interests include uncertainty analysis and optimization of integrated energy systems.

Yue Pan received the B.S. degree in electrical engineering from the Hunan University, Changsha, China, in 2021, and the M.S. degree with the School of Electric Power Engineering, South China University of Technology, Guangzhou, China, in 2024. Her research interest includes uncertainty optimization of integrated energy systems.

Weikun Liang received the B.S. and Ph.D. degrees in electrical engineering from South China University of Technology, Guangzhou, China, in 2020 and 2025, respectively. His research interest includes uncertainty optimization of integrated energy systems.

Mingbo Liu received the B.S. degree from the Huazhong University of Science and Technology, Wuhan, China, in 1985, the M.S. degree from the Harbin Institute of Technology, Harbin, China, in 1988, and the Ph.D. degree from Tsinghua University, Beijing, China, in 1992. He is currently a Professor with the South China University of Technology, Guangzhou, China. His research interests include energy management and operation control of power systems.